BASIC SCIENCE

Nanomedicine: Nanotechnology, Biology, and Medicine
13 (2017) 1519–1529

Original Article

nanomedjournal.com

Real-time liver uptake and biodistribution of magnetic nanoparticles determined by AC biosusceptometry

Caio C. Quini, PhD[a,*], André G. Próspero, MSc[a], Marcos F.F. Calabresi, PhD[a], Gustavo M. Moretto, MSc[a], Nicholas Zufelato, MSc[b], Sunil Krishnan, MD[c], Diana R Pina, PhD[d], Ricardo B. Oliveira, MD[e], Oswaldo Baffa, PhD[f], Andris F. Bakuzis, PhD[b], Jose R.A. Miranda, PhD[a]

[a]*Laboratório de Biomagnetismo, Departamento de Física e Biofísica, IBB, Univ. Estadual Paulista, Botucatu, São Paulo, Brazil*
[b]*Instituto de Física, Federal University of Goiás, Goiânia, Brazil*
[c]*Department of Experimental Radiation Oncology, University of Texas, MD Anderson Cancer Center, Houston, TX, USA*
[d]*Departamento de Doenças Tropicais e Diagnóstico por Imagem, Faculdade de Medicina de Botucatu, Univ. Estadual Paulista, Botucatu, São Paulo, Brazil*
[e]*Faculdade de Medicina de Ribeirão Preto, São Paulo University, Ribeirão Preto, São Paulo, Brazil*
[f]*Departamento de Física, Faculdade de Filosofia, Ciências e Letras de Ribeirão Preto, São Paulo University, Ribeirão Preto, São Paulo, Brazil*

Received 22 November 2016; accepted 5 February 2017

Abstract

We describe the development of a joint *in vivo/ex vivo* protocol to monitor magnetic nanoparticles in animal models. Alternating current biosusceptometry (ACB) enables the assessment of magnetic nanoparticle accumulation, followed by quantitative analysis of concentrations in organs of interest. We present a study of real-time liver accumulation, followed by the assessment of sequential biodistribution using the same technique. For quantification, we validated our results by comparing all of the data with electron spin resonance (ESR). The ACB had viable temporal resolution and accuracy to differentiate temporal parameters of liver accumulation, caused by vasculature extravasation and macrophages action. The biodistribution experiment showed different uptake profiles for different doses and injection protocols. Comparisons with the ESR system indicated a correlation index of 0.993. We present the ACB system as an accessible and versatile tool to monitor magnetic nanoparticles, allowing *in vivo* and real-time evaluations of distribution and quantitative assessments of particle concentrations.

Key words: AC biosusceptometry; Magnetic nanoparticles; Biomedical instruments; Real time monitoring; Quantification methods; Nanoparticle uptake

Nanomedicine is a broad term used to describe nanotechnology applications for the health sciences.[1,2] Nanotechnology improves system sensitivity,[3–6] enables cell labeling and detection, and allows the monitoring of biological processes.[3,7–9] The application of nanotechnology for both diagnosis and therapy using the same modality confers nanomaterials with extraordinary theranostic potential, enabling their application as molecular probes, enhancers of imaging sensitivity and specificity,[8,10,11] therapeutic agents in the form of highly specific drug delivery systems,[12,13] hyperthermia probes,[14–16] and combinations thereof.[17]

According to the United States Food and Drug Administration and the Alliance for NanoHealth, the necessity to properly monitor these nanostructured agents after systemic injection and tracking them inside biological systems over time are among the main challenges for translating nanomedicine into patient treatment.[18]

To explore their translational potential, pharmacokinetics and biocompatibility parameters must first be characterized and optimized.[18–20] Therefore, it is crucial to search for methods that allow the dynamic monitoring of their distribution after administration and assess accumulation patterns in organs of interest.[18,21]

Funding: This work was supported by the Sao Paulo Research Foundation (FAPESP; grant no. 2010/07639–9, 2011/18696–6, 2013/20842–6, and 2015/14914–0).

*Corresponding author.
E-mail addresses: caioquini@ibb.unesp.br, caioquini@gmail.com (C.C. Quini).

http://dx.doi.org/10.1016/j.nano.2017.02.005
1549-9634/

The time that takes for nanoparticles to be cleared from the bloodstream and their destination are extremely important parameters for *in vivo* tests and preclinical studies[2,22] because they allow the generation of nanoparticle biocompatibility profiles.[23] However, the *in vivo* monitoring and quantification of these nanostructures, because of their inherent properties, remain a challenge.[3]

Despite variations in biodistribution patterns, the lungs and spleen generally retain most of the particles, ranging from 200 to 1000 nm, whereas the kidneys rapidly eliminate nanostructures smaller than 8 nm[24]. The liver is mainly responsible for the uptake of nanoparticles within the range of clinical applications. Resident macrophages in the reticuloendothelial system remove these structures almost instantaneously from the bloodstream.[7,23–25] This specific pattern makes the liver a target for nanoparticle accumulation, followed by spleen and bone marrow, which are organs with high levels of macrophages.[6,7,26–28]

Numerous studies have reported new conjugation and targeting strategies that seek to enhance nanotechnology efficiency. However, few studies have sought to develop efficient detection modalities to investigate their biological profile in animal models.[26,29]

Nanoparticles can be detected and visualized either due to its inherent properties, such as x-ray fluorescence (based on characteristic x-ray emission),[30] Magnetic Resonance Imaging (MRI) scans,[3,8,11] Magnetic Particle Imaging (MPI),[31,32] absorbance and scattering imaging based techniques, or *via* conjugation to imaging contrast agents, such as near infrared (NIR) fluorescent materials, or radioactive markers, by positron emission tomography (PET), or single photon emission computed tomography (SPECT).[3,33]

Although many studies have reported nanoparticle detection in an attempt to monitor their distribution within biological systems, most of these have failed to provide quantitative information or proper temporal resolution.[3,26,34] Alternating current biosusceptometry (ACB) is a biomagnetic detection system, extensively employed in gastroenterology assessments in both animal and human studies.[35–39] The technique is relatively inexpensive, portable, and versatile, allowing noninvasive investigations of physiological patterns *in vivo* and in real time with quantitative analyses of magnetic nanoparticle (MNP) concentrations in samples.[40]

In the present study, we used a joint ACB approach to evaluate dynamic MNP liver accumulation associated with MNP biodistribution patterns. We assessed liver uptake and its response to changes in the dose and administration protocols of citrate-coated manganese ferrite (Ci-$MnFe_2O_4$) nanoparticles. We also evaluated the biodistribution profiles of different doses, administration protocols, and times. To validate the ACB technique as a quantitative method, we also analyzed all of the biodistribution data using electron spin resonance (ESR) spectroscopy.

Methods

AC biosusceptometry

The ACB system has been previously described[35,41] and is illustrated in Figure 1. It works as a double magnetic flux transformer with two identical pickup coil pairs that are arranged on a first-order gradiometric configuration, in which one pair (excitation/detection), farther from the sample works as a system reference. The excitation coils generate an AC magnetic field, inducing current into the detection coils at a constant rate. When no magnetic material is near the measurement probe (detector), the response is minimized because both pairs (reference and detection) have the same setup. Once a magnetic sample approaches the detector, an imbalance in the magnetic field is created, changing the magnetic flux and consequently the electrical current that is induced into the detector coil. This signal can be acquired through a phase-sensitive amplifier (lock-in – Stanford Research Systems SR830), digitized, and recorded online (Figure 1).

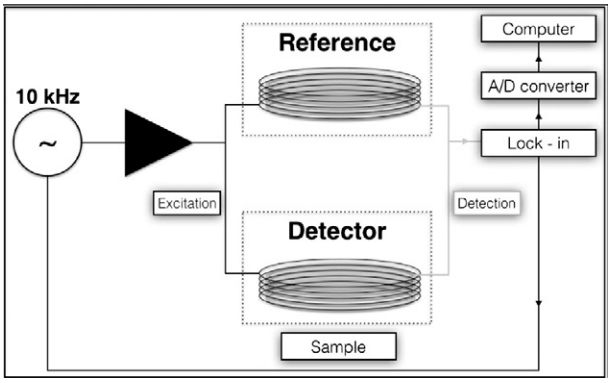

Figure 1. Illustration of ACB settings.

The physical setup of the AC biosusceptometer that was employed herein consisted of two identical detection pickup coils (500 turns of copper wires; 10 mm diameter, 10 mm width) and two excitation coils, connected directly in series (150 turns of copper wire; 14 mm diameter, 10 mm width), generating an alternating magnetic field (2 mT – rms, 10 kHz). The excitation coils were turned over the sensing coils. Both reference and detection coil pairs were composed of an excitation coil (outer) and sensing coil (inner) and were separated by a baseline (150 mm) that provided a good signal-to-noise (SNR) ratio.

The operational frequency was chosen after evaluating the SNR ratio and the Common-mode Rejection (CMR) Rate of the system (due to the gradiometric configuration). The increase in frequency improves the SNR and deteriorates the CMR, since the offset voltage of the system increases. These parameters are dependent on intrinsic features of each system, namely wire diameter, number of turns, radius and thickness of each coil. Such characteristics will determine resistance, capacitance and inductance of the ACB sensor. Therefore, depending on their specifications, each sensor will have a slight variation around 10 kHz to ensure good sensitivity. The field strength is, therefore, limited in 2mT due to all of these parameters chosen, specially the CMR.

It is noteworthy that these features do not have any relation with the signal acquired. All parameters are chosen aiming to improve sensitivity, SNR and CMR, which in turn allow us to quantify a significant small number of particles per sample, as our results indicates.

Any magnetic material near the detection probe can sensitize the ACB device because it can influence the magnetic flux that is

generated by the excitation coil. This affects the electrical current inductance upon the detector coil, which depends on the material's susceptibility, concentration, and position. This relationship between magnetic flux (Φ_d) and the sample near the probe can be explained by

$$\Phi_d = \frac{1}{\mu_0 I_d} \int \chi\left(\vec{r}\right) \overrightarrow{B_a} . \overrightarrow{B_d} \; dV \quad (1)$$

where μ_0 is the magnetic permeability in the vacuum, I_d is the induced electrical current in the detector coils, χ is the sample magnetic susceptibility, $\overrightarrow{B_a}$ is the applied magnetic field, and $\overrightarrow{B_d}$ is the reciprocal field, generated by the induced current in the detector coils.[41,42]

The magnetic flux, therefore, is determined by a relationship between the intrinsic features of the biosusceptometer (*i.e.*, applied current, excitation and detection coil specifications) and sample characteristics (*i.e.*, magnetic susceptibility, volume, and distance from the sensor).[41]

Thus, we can relate the magnetic signal obtained with the analyzed sample position and concentration, which in our case corresponded to the position distribution and concentration of the MNPs in organs and tissues of interest.

Magnetic nanoparticles

Among the so-called nanovehicles, superparamagnetic iron oxide nanoparticles (SPIONs) have drawn attention because of their application as contrast agents for magnetic resonance imaging (MRI)[43,44] and their influence on T2-weighted imaging. These particles also allow conjugation to specific agents, thus creating efficient drug delivery systems,[3,7–9] with the ability to be applied as heat generator, when interacting with an alternating magnetic field.[14–16,45] Because of these properties, this material is among the best examples of nanotheranostic agents.

In the present study, we employed Ci-$MnFe_2O_4$ nanoparticles, synthesized by a co-precipitation method, previously described[14] and characterized.[40] This Mn-doped iron oxide nanoparticle was chosen because of its excellent low-field magnetic response and interesting properties with regard to MRI and hyperthermia applications.[46–48] Their hydrodynamic diameter and Zeta potential were 13 ± 4 nm and – 27.8 mV, respectively, at pH 7.4[14,40]. The Ci-$MnFe_2O_4$ nanoparticles presented a saturation magnetization of 264 kA/m and showed superparamagnetic behavior (see Figure 4 of Ref.[40]). These MNP properties associated with magnetic field features of the ACB system (field amplitude of 2 mT and 10 kHz frequency) make this technique a harmless monitoring method, allowing us to work considerably below the Atkinson's (field/frequency limit) criteria and within the linear magnetization response regimen.[49]

Electron spin resonance

To validate the ACB method, we performed a comparison study by assessing all of the biodistribution data using both the ACB and ESR systems. Electron spin resonance spectroscopy can quantify the number of spins that are present in a given tissue that might originate from free radicals, paramagnetic substances, and even MNPs within the sample.[50–53]

The ESR spectra depend on the free-electron spin concentration and environment, which are material-dependent.[20] In the present study, we acquired MNP concentrations by measuring the area under the curve for the intensity absorption spectrum (centered in g = 2), which is related to the amount of resonant spins in the sample and thus related to the MNP concentration.[20,22,50–52]

All of the biodistribution samples were first evaluated by the ACB system and then analyzed by a JEOL ESR – X band spectrometer (JES – FA 200[9.5GHz]) under the same conditions and same parameters (temperature, 18 °C; microwave power, 0.998 mW; microwave frequency, 9450.051 MHz; field range, 186–486 mT, centered in 336 mT; modulation amplitude, 0.2 mT; time constant, 0.03 s; 10× gain for heart and kidneys samples [for which we expected a lower MNP accumulation profile] and 5× gain for all other organs). This step allowed us to validate all of the quantitative measurements regarding MNP concentrations in the organs of interest.

Experimental setup

Dynamic liver accumulation of MNPs determined by AC biosusceptometry

All of the animal experiments were conducted according to the São Paulo State University (UNESP) Committee for the Use and Care of Animals (protocol no. CEUA – IBB 409).

We assigned 16 male rats (*Rattus norvegicus albinus* [Wistar]; Anilab, Paulinia, SP, Brazil), weighing 250–300 g, to four groups that received the following: saline (0.9 mg/ml; control) and one (G1), two (G2), and three (G3) 300 μl injections of MNPs (23 mg/ml, 1.17×10^{15} nanoparticles/ml, dispersed in saline solution). The MNP concentration was carefully chosen by considering both safety and feasibility. We sought an optimal relationship between synthesis protocol and biological application, especially concerning the minimum dose that would still provide a good ACB signal-to-noise ratio.[48,54,55] No animal experienced any adverse effect due to MNP injection nor dyed during the experiment.

To assess how the injection protocol may interfere with the accumulation pattern, four additional rats (G4) received a single MNP injection of 900 μl. This step allowed us to compare the accumulation pattern with the results from G3, which received three MNP injections (for a total of 900 μl).

We acquired the uptake process in real time, actively capturing MNPs in the liver. We recorded the ACB signal for 30 min after each MNP injection, regardless of the number of injections that each animal received in the G1, G2, and G3 groups. For the G4 group, we recorded the ACB signal for 90 min. This protocol was necessary to compare the accumulation patterns between groups and assess the influence of the administration protocol on this profile. We did not register any ACB signal modification that corresponded with the saline solution. Therefore, this group was excluded from the statistical comparisons and was used only as a proof of concept to indicate the specificity of ACB for the magnetic materials.

All of the animals received the MNPs intravenously through the left femoral vein using a cannulation procedure. After anesthesia with 99% urethane (1.5 mg/kg) and positioning the animals, we placed the ACB sensor over the abdominal region on

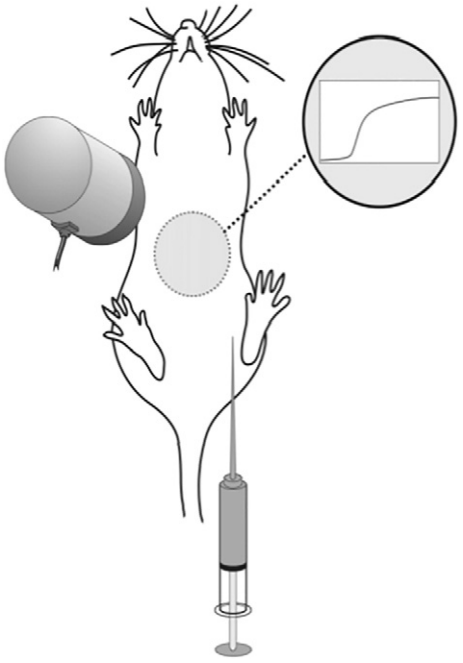

Figure 2. Experimental setup for MNP injections and ACB monitoring, illustrating the animal and ACB, positioned over the liver projection in the abdominal region (marked by the gray circle).

the liver projection. Figure 2 shows the experimental setup for the nanoparticle injection protocol, indicating intravenous administration followed by the dynamic monitoring procedure.

Pharmacokinetic assessment

The MNP accumulation pattern is a multifactorial process influenced by physiology and features of the nanoparticles.[24,29] To evaluate the MNP pattern in the liver, we employed a mathematical model based on three compartments. We considered the circulation system as a single compartment (x_1) and divided the liver uptake process into two separate profiles (nanoparticle extravasation [x_2] due to fenestrated vasculature and macrophage action [x_3]):

$$\frac{dx_1}{dt} = x_1'(t) = -K_1.x_1 + K_2.x_2 \quad (2)$$

$$\frac{dx_2}{dt} = x_2'(t) = +K_1.x_1 - K_2.x_2 - K_3.x_2 \quad (3)$$

$$\frac{dx_3}{dt} = x_3'(t) = +K_3.x_2 \quad (4)$$

where K_1, K_2, and K_3 represent the flux coefficient among each compartment. We considered the initial time point for the model when the entire MNP dose was injected, indicating the instant when all of the particles were present in x_1 ($x_1[0] = C_{MAX}$ = Maximum concentration), so there were no MNPs in the liver ($x_2[0] = x_3[0] = 0$). Notably, the present system of equations assumes a simplified model that considers only liver uptake. We also did not consider excretion parameters[22,24] because we evaluated relatively short time intervals. Considering these initial conditions, the solution for the equation system can be expressed as a sum of two independent, although complementary, accumulation factors. In this approximation, the ACB signal ($Y(t)$), which is proportional to the total amount of nanoparticles in the liver at each instant, can be modeled using the following equation:

$$Y(t) = Y_0 + A_1\left[1 - e^{-t/\tau_1}\right] + A_2\left[1 - e^{-t/\tau_2}\right] \quad (5)$$

where Y_0 corresponds to the initial value (*i.e.*, the ACB signal immediately before the injection). After fitting the magnetic signal, we recorded A_1, τ_1, A_2, and τ_2 for each administration.

This first-order equation system provides a solution with two average accumulation exponential coefficients (τ_1 and τ_2) and also two uptake indices (A_1 and A_2) that, when summed, represent the total MNP accumulation at each instant t in the organ. These coefficients are dependent on all K_i constants and concentration of the nanoparticles injected. After assessing the data that were obtained fitting our signal with this model, our results suggested signal dependency on two distinct growing factors that, when summed together, represented liver uptake. The mathematical modeling was acquired using Maple 13, and all fitting parameters were acquired in OriginLab 8.5.

After the experimental procedure, we euthanized the animals and collected a blood sample and the liver, spleen, lungs, heart, and kidneys from each animal to perform the biodistribution study. This setup allowed us to assess accumulation and biodistribution patterns in the same animals.

Ex vivo biodistribution by ACB

Influence of dose and administration protocols on biodistribution patterns

For the quantification process, we randomly selected a 100 mg portion of each lyophilized organ from each group and stored it in a volume-controlled flask. We placed the flask containing the sample on the sensor surface and recorded the signal intensity, repeating this procedure three times for each sample.

An important issue is whether same doses, administered using different injection protocols, result in different MNP accumulation patterns. Thus, four rats in the G4 group received a single MNP administration of 900 μl, which allowed us to compare the accumulation pattern with the results from G3, which received three MNP injections for a total of 900 μl.

Influence of time on biodistribution patterns

We divided 16 male rats into four groups (1, 4, 16, and 24 h). Each animal received a single injection of 300 μl MNPs *via* femoral vein. The animals were then euthanized by decapitation at the time point that corresponded to its respective group. Organ collection, sample preparation, and measurement protocol were the same as in the previous experiments.

Calibration curve protocol

The main objective of this step was to provide *ex vivo* quantitative information about *in vivo* particle distribution and accumulation. Thus, we built a calibration curve (Figure 4) to compare the results that were obtained from the ACB response to

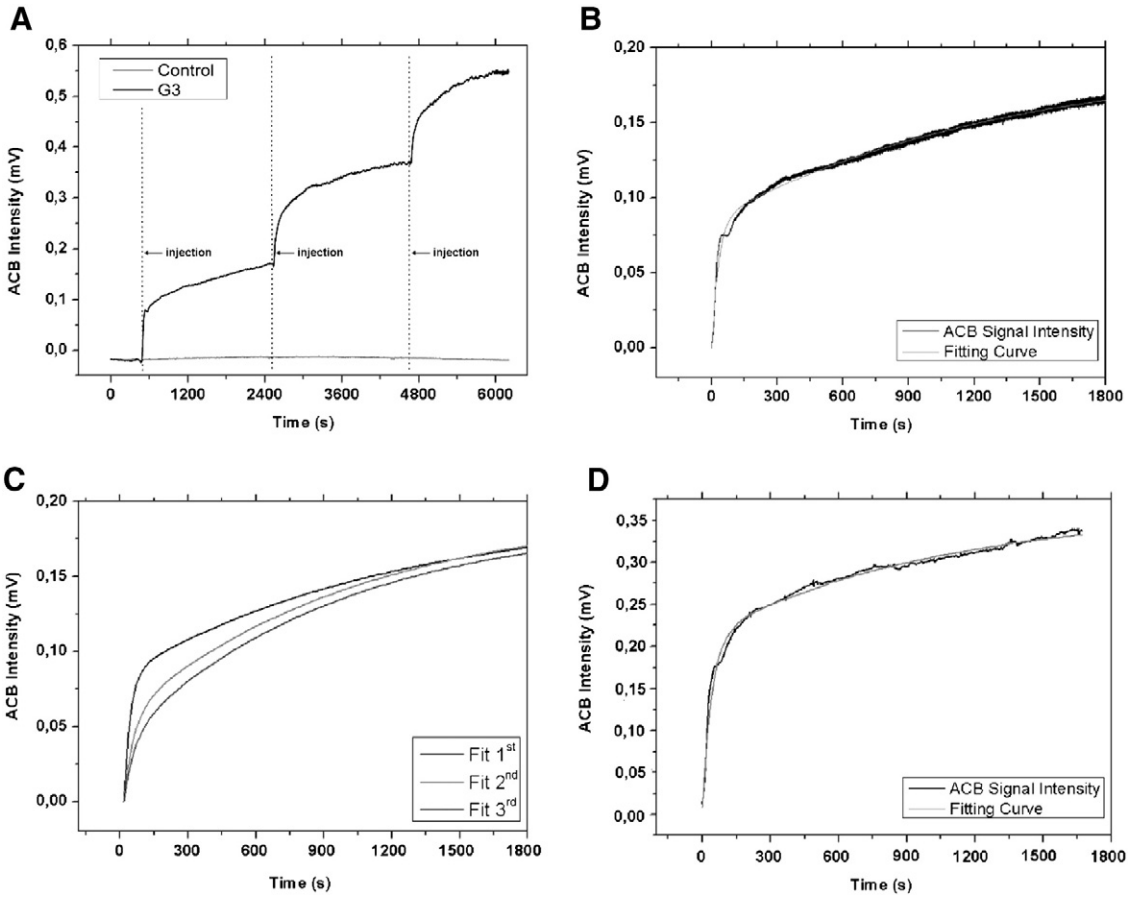

Figure 3. ACB signal acquired from G3. (**A**) Raw signal obtained during the injection procedure compared with the saline injection in the control group. (**B**) Fitting procedure that we employed for each curve. (**C**) Representation of the double exponential fitting curve for all three injections, starting from the same time point and amplitude. (**D**) Single MNP injection (900 μl) in G4.

a known concentration of samples, wherein we had a well-established number of MNPs.

We diluted our stock MNP batch (originally 23 mg/ml, 1.17×10^{15} nanoparticles/ml) into seven vials with different concentrations but the same volume. This step allowed us to compare the ACB signal response to known MNP concentrations. Considering the signal dependency on intrinsic properties of both the sensor and sample and while maintaining the sample volume, probe-sample distance, and ACB acquisition setup constant, the only parameter that changed was the sample magnetic susceptibility (χ). The ACB signal intensity, therefore, was exclusively dependent on the number of particles per sample, which enabled quantification for all of the *ex vivo* samples.

Signal quantification and statistical analysis

The data are expressed as the mean ± standard deviation. All of the statistical analyses were performed using GraphPad Prism software. For the validation experiment for both the ACB and ESR techniques, we evaluated the signal intensity difference between injections and between time-points using one-way analysis of variance (ANOVA) followed by Tukey *post hoc* test and linear trend analysis. For comparisons of the injection protocols, we used two-way ANOVA followed by Bonferroni *post hoc* test.

We compared all of the ACB signals that were obtained from each *ex vivo* sample to their respective ESR results for each organ and each animal in all of the groups. This comparison was performed using paired *t*-tests. Values of $p < 0.05$ were considered statistically significant.

Results

Dynamic liver accumulation of MNPs determined by AC biosusceptometry

Figure 3 illustrates the dynamic evaluation process. Figure 3*A* shows an example of the acquired ACB signal for the control and G3 groups. This signal pattern corresponded to the increasing concentrations of nanoparticles in the liver after each injection. The data from the control group showed no increase. Figure 3*B* shows the fitting curves for such processes, which allowed us to assess the dynamic accumulation pattern. For comparison purposes, in Figure 3*C*, we disregarded both the injection time and initial signal amplitude before administration and present the ACB signal obtained from all three injections, starting from the same point. Figure 3*D* illustrates the accumulation profile for a single injection of 900 μl (G4).

All of the fitting coefficients (A_1, A_2, τ_1, and τ_2) and accumulation factor ($A_1 + A_2$) after each administration for G1, G2, and G3 are presented in Table 1.

Table 1
Average fitting parameters acquired (± standard deviation).

	MNP Injection	τ_1 (s)	A1 (mV)	τ_2 (s)	A2 (mV)	A1 + A2 (mV)	*n*
Injections	First	35 ± 8[a]	0.096 ± 0.021[a]	1539 ± 361.2[a]	0.138 ± 0.014[a]	0.234	9
	Second	40 ± 15[a]	0.076 ± 0.030[a]	874.4 ± 284.8[b]	0.145 ± 0.013[a]	0.221	6
	Third	32 ± 3[a]	0.070 ± 0.024[a]	703.1 ± 107.2[b]	0.165 ± 0.108[a]	0.235	3

	Groups	Injections	A1 (mV)		A2 (mV)		*n*
Protocols	G3	First	0.096	∑ = 0.213	0.138	∑ = 0.451	3
		Second	0.076		0.148		
		Third	0.070		0.165		
	G4			0.201		0.150	3

Different letters indicate significant differences within columns ($p < 0.05$).

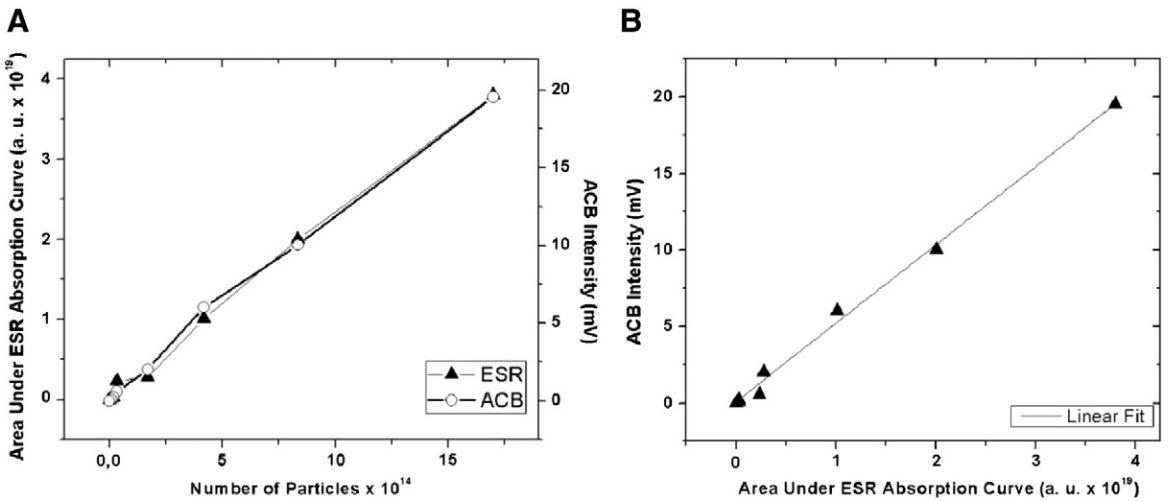

Figure 4. *In vitro* comparison of the ACB and ESR signals for the same particle concentrations (**A**) and correlation between ACB and ESR (**B**).

Table 1 shows that the average τ_1 coefficient presented no variation over sequential administrations, whereas A_1 decreased. Although the decrease in amplitude was not statistically significant, it showed a linear trend ($R^2 = 0.209$), suggesting a decreasing pattern. The second growth factor did not show any significant change. Both coefficients, however, showed a linear tendency profile (τ_2: $R^2 = 0.499$; A_2: $R^2 = 0.308$), indicating that the time decreased and the amplitude increased for sequential administrations.

Injection protocol: comparison between G3 and G4

Figure 3*D* shows the ACB signal intensity obtained from the G4 with the respective fitting curve. Table 1 shows the average fitting coefficients for G4, accompanied by a comparison of the fitting coefficients between G3 and G4. Table 1 also shows that the G4 group, which received a single MNP injection of 900 μl, had a notably higher A_1 factor, suggesting a sinusoidal increase in accumulation, whereas the parameters that were acquired from the second exponential factor (A_2) were similar to the G3.

Ex vivo biodistribution determined by ACB

Calibration curve and ESR validation procedure

Figure 4 presents the results from the calibration curve for both the ESR and ACB systems (Figure 4*A*), followed by the correlation between both methods (Figure 4*B*). The signal intensity linearly changed as the particle concentration increased.

These data indicated a very strong correlation between techniques ($R^2 = 0.993$) and allowed us to quantify the MNP concentration *ex vivo* in tissue samples. All of the samples that were measured *ex vivo* in the ACB were also analyzed by the ESR for validation purposes.

Influence of dose and administration protocols on biodistribution pattern dose

Figure 5 shows the biodistribution results, including the number of particles that were found in each organ in G1, G2, and G3 by ACB and ESR methods.

We compared the results obtained from both systems for each organ using paired *t*-tests. This analysis indicated no significant variations between systems for all of the samples. All of the groups presented an increase in accumulation in the spleen, liver, and blood for shorter time points. However, 4 h after the MNP injection, the particle blood concentration approached zero.

Administration protocol

Figure 5*C* and *D* show the ACB and ESR signal intensities that were acquired from the organs that were collected from the

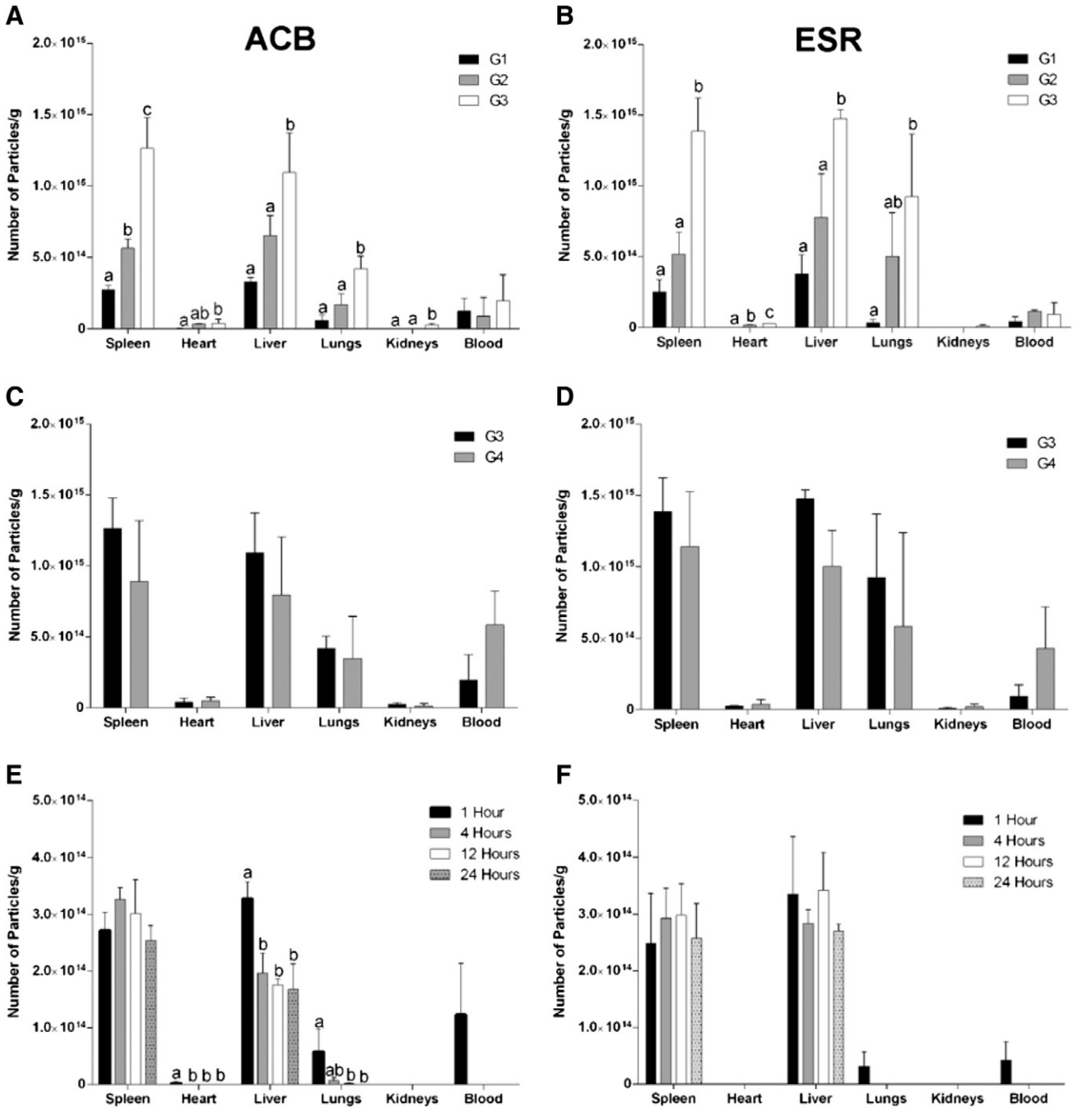

Figure 5. (**A**) ACB and (**B**) ESR data for MNP biodistribution in G1, G2, and G3. (**C**, **D**) Comparison between G3 and G4 for the ACB (**C**) and ESR (**D**). (**E**, **F**) Biodistribution results and changes due to time for ACB (**E**) and ESR (**F**). The results are expressed as mean and standard deviation. Same letters represent no significant difference, whereas different letters indicate significant differences between groups ($p < 0.05$).

G3 and G4 groups. Although no significant differences were found between groups, they suggested apparently lower accumulation in the liver and spleen and higher concentrations in blood in the G4 group, indicating a different uptake profile for the single dose. When we evaluated the results for each organ separately, no significant difference was found between the ACB and ESR techniques.

Influence of time on biodistribution patterns

Figure 5*E* and *F* present the ACB and ESR signals that were acquired from each sample with regard to the number of particles per sample. Figure 6*A* shows an example of ESR spectra that were obtained from liver samples from four animals in each group (1, 4, 12, and 24 h after MNP administration).

Discussion

The present real-time *in vivo* study investigated the liver accumulation of SPIONs and changes in this parameter that were caused by different administration protocols. We applied the same technique to quantitatively assess the way in which these changes influenced biodistribution patterns. All of the quantitative data were compared with a gold standard technique (ESR), which indicated the reliability of our method.

Although many studies have reported the uptake process as a multi-compartment phenomenon,[22] the liver alone is generally responsible for the retention of more than 90% of the dose that is injected.[7] Thus, monitoring the liver uptake process was a logical first step in generating a correlational model between real-time accumulation and overall biodistribution pattern.

We consider that two main mechanisms are responsible for the liver uptake of MNPs. The noncontinuous hepatic endothelium with fenestrated vasculature leads MNPs to extravasate into hepatic sinusoids, resulting in nonspecific particle accumulation. Afterward, the uptake process is completed by macrophage endocytosis, which depends on several intrinsic factors, including particle size, shape, and charge, among others.[2,26,29,56]

A_1 represents the maximum particle concentration to be retained in parenchymal tissue, and τ_1 refers to the average time that it takes for the filtration process to occur. Sequential injections might have overloaded uptake by sinusoidal tissues, thus causing a decrease in A_1. However, τ_1 depends on blood flow, which did not change during the injections, thus causing the temporal parameter to remain constant.

By applying these coefficients to Eq. (1), we could construct and predict a profile for the retention pattern. Both growth parameters (A_1 and A_2) influenced the entire curve, although the first factor (related to smaller t values) was more relevant for the initial rise, whereas the second factor (greater t value) played a more important role in the final part, in which the exponential growth pattern was considerably less intense. We can relate the double exponential fitting curve to this double factor uptake profile. Thus, we associated the first growth factor (more rapid and intense) to the extravasation process, whereas the second factor was related to the action of macrophages, which provided the later effect on the accumulation pattern.

With regard to dose variations, the fitted lines in Figure 3*C* indicated that the accumulation process was slowing, suggesting interference from some saturation process. However, after sequential MNP injections, τ_2 decreased and A_2 increased, suggesting an enhancement of macrophage actions that removed particles from the hepatic parenchymal region. Nonetheless, the final signal amplitude (*i.e.*, total uptake after each injection) was maintained, indicating compensatory actions of macrophages that were initiated when the first system was saturated.

When we compared the A_1 coefficients from G4 with the sum of all A_1 factors that were obtained from G3, the values were very close, indicating that the liver filtration properties were preserved after both protocols. However, the sum of all three A_2 coefficients showed a significantly higher intensity for the G3 compared with G4.

Considering that the actions of macrophages are limited by the number of available cells in the system and their individual function,[25] a multiple injection protocol would spare some macrophages and give the reticuloendothelial system time to recover before the next MNP administration. In contrast, a single injection would sensitize the entire system at once.

The present study found considerable differences in the accumulation process, especially with regard to the average uptake time and particle concentration when we increased the number of injections (dose). Modification of the administration protocol showed that this parameter can be optimized to preserve liver retention or saturate it and reduce the rate of accumulation, which is an important consideration regarding the purpose of the administration.

The biodistribution study indicated an expected higher signal for the liver and spleen samples after the injections. Figure 5*A* and *B* show significant differences between the first, second, and third injections for the spleen. The signal acquired from the liver samples was not significantly different after the three injections. Nonetheless, the results indicated a linear growth tendency, with a significant increase in the signal after the third injection.

This pattern also suggests that the general retention process was not saturated after sequential injections. Figure 5*A* and *B* show a linear growth tendency following each MNP injection for all of the organs in the dynamic accumulation study, supporting the hypothesis that the actions of macrophages compensate for the lower parenchymal accumulation after sequential injections.

Both the ACB and ESR systems indicated increases in liver and spleen accumulation in G3, whereas the MNP concentration in blood was lower compared with G4. The greater number of particles in the blood samples in G4, together with the lower retention in the liver, suggest lower liver retention in these animals. These data support our hypothesis that the higher dose caused macrophage saturation at this specific time point.

At 1 h, in addition to the expected higher signals that were obtained from the liver and spleen, some particles were still circulating, reflected by the high signal for the blood samples. This high MNP concentration in the bloodstream may be responsible for the significantly greater number of particles in the liver samples and lungs that were detected by the ACB system. Additionally, the ACB results showed a considerable decrease in signal after the first hour, which was not confirmed by the ESR data. This apparent discrepancy might be attributable to the formation of aggregates. The ACB technique excites nanoparticles with a field amplitude of 2 mT. Therefore, if the particles that arrive in the liver form complex structures (*e.g.*, spherical-like aggregates with flux-closure moment configurations), then one might expect that such a low field amplitude would not excite a certain number of nanoparticles. This might explain the difference in the absolute values that were obtained by the ESR technique because it counts the number of unpaired spins, which are unaffected by such an aggregation state.

Indeed, the ESR field is susceptible to particle aggregation, as discussed by others.[14,57] Figure 6*B* shows the resonance field for the ESR signals from each group as a function of time. The decrease in the resonance field indicates particle-particle interactions, which may explain the decrease in the ACB signal and might indicate the desorption of citrate from the nanoparticle surface inside the organ. Additionally, this signal response profile obtained by the ACB system might be an important tool for determining particle integrity and aggregation states.

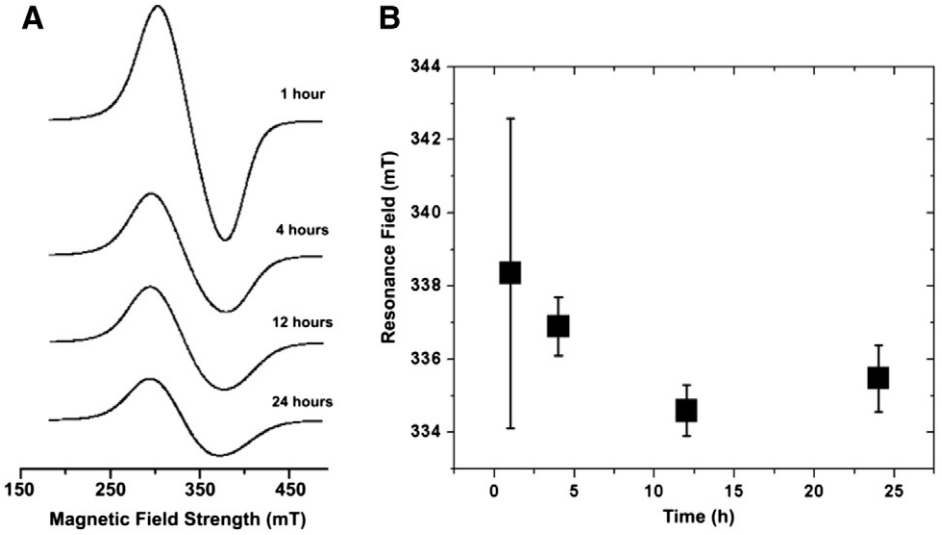

Figure 6. (**A**) Typical ESR spectrum obtained from the liver at each time point. (**B**) Average peak width obtained from each group (1, 4, 16, and 24 h).

Four hours after administration, no circulating particles were detected, and the spleen presented its highest value. The ACB signal from the liver decreased significantly from its previous intensity, whereas the ESR signal did not present significant variations within the experimental time window. Because these results were incongruent, we could not determine whether a clearance process began at this time point.

We can assume, however, the existence of a biological process that alters nanoparticle or iron concentrations inside the organ. The ESR signal of MNPs that were centered in g = 2 might be influenced by Fe^{3+} ferritin ions centered in g = 2.1[19], which could interfere with system detection and thus hamper the detection of subtle variations in the magnetic signal.[53] Another possibility could involve initial particle biodegradation. Such biodegradation process would decrease the particle size and consequently the ACB magnetic signal because the sensitivity of the system strongly depends on particle size. However, some evidence suggests that this process occurs over longer periods of time and not within 24 h.[22,26]

Thus, an alternative hypothesis could involve an effect of nanoparticle agglomeration, which would decrease equilibrium susceptibility because of the presence of flux-closure aggregates. In this case, the nanoparticle arrangements would not be able to respond to this low field amplitude of the ACB system and consequently would not contribute to the magnetic signal. Such a decrease in susceptibility has recently been reported for magnetoliposomes, which might be considered a model system for the effect of nanoparticle endocytosis.[58] In contrast, the ESR signal would not drop because the number of unpaired spins, detected by the ESR system, is unaffected by particle organization. Further studies focusing on this parameter and analyzing longer time points are needed for a proper evaluation of this profile.[22] These findings suggest that a joint approach that utilizes the ACB system for rapid biodistribution analyses and dynamic evaluations might help achieve a more complete pharmacokinetic assessment of nanoparticles after intravenous administration.

Nanotherapeutic approaches need to overcome several hurdles before being considered reliable and effective for clinical application. Major efforts have been made to improve their interactions with biological barriers. Innovative synthesis and conjugation strategies, combined with more rational approaches, are needed to overcome such biological limitations.[29] Regardless of the level of nanostructure complexity, this problem needs to be properly addressed. Developing techniques to effectively monitor nanoparticles within biological environments is also crucial.

Conclusion

In this study, we performed a non-invasive, dynamic evaluation on MNP accumulation with direct relation to biodistribution assessment. Our results showed that sequential injections induce different accumulation rate, although these modifications did not change significantly the biodistribution profile. This result was confirmed by the *ex vivo* biodistribution study, which showed that, under physiological conditions, the administration protocol will not change the final destination of nanoparticles. It will, however, influence significantly the uptake rate and, possibly, their pharmacokinetic properties. The biodistribution data showed the same linear behavior observed in the calibration curve and the accumulation pattern was preserved for all of the three doses chosen. On regards to time, our study obtained an expected higher accumulation in liver and spleen, with an unexpected signal decrease after one hour. This is a strong indicative for particle agglomeration. However, studying such interaction was not in the scope of our study and should be addressed properly in further assessments. Considering the current demand for adequate nanoparticle monitoring techniques, we applied the ACB system as an analytical tool to gather, in real time, *in vivo* information about MNP concentrations using quantitative *ex vivo* assessments with the same system and the same sensor probe. The validation protocol, performed against a standard technique, which has

been employed on quantification studies, physicochemical analyses and cell interaction assays, allows us to forecast future applications using the ACB device as a biosensor probe for cellular uptake studies. ACB technology has already been employed in several animal and human studies, and we strongly believe that the ACB system will take us one step closer to the application of nanoparticles for patient treatment.

References

1. Peer D, Karp JM, Hong S, Farokhzad OC, Margalit R, Lange R. Nanocarriers as an emerging platform for cancer therapy. *Nat Nanotechnol* 2007;**2**:751-60.
2. Lee MJ-E, Veiseh O, Bhattarai N, Sun C, Hansen SJ, Ditzler S, et al. Rapid pharmacokinetic and biodistribution studies using cholorotoxin-conjugated iron oxide nanoparticles: a novel non-radioactive method. *PLoS One* 2010;**5**:e9536.
3. Thomas R, Park I-K, Jeong YY. Magnetic iron oxide nanoparticles for multimodal imaging and therapy of cancer. *Int J Mol Sci* 2013;**14**:15910-30.
4. Wabler M, Zhu W, Hedayati M, Attaluri A, Zhou H, Mihalic J, et al. Magnetic resonance imaging contrast of iron oxide nanoparticles developed for hyperthermia is dominated by iron content. *Int J Hyperthermia* 2014;**30**:192-200.
5. Parka YC, Smitha JB, Phama T, Whitakera RD, Sucatoa CA, Hamilton JA, et al. Effect of PEG molecular weight on stability, T2 contrast, cytotoxicity, and cellular uptake of superparamagnetic iron oxide nanoparticles (SPIONs). *Colloids Surf B Biointerfaces* 2014;**119**:106-14.
6. Sun C, Lee JSH, Zhang M. Magnetic nanoparticles in MR imaging and drug delivery. *Adv Drug Deliv Rev* 2008;**60**:1252-65.
7. Cole AJ, David AE, Wang J, Galbán CJ, Yang VC. Magnetic brain tumor targeting and biodistribution of long-circulating PEG-modified, cross-linked starch-coated iron oxide nanoparticles. *Biomaterials* 2011;**32**:6291-301.
8. Chertok B, Moffat BA, David AE, Yu F, Bergemann C, Ross BD, et al. Iron oxide nanoparticles as a drug delivery vehicle for MRI monitored magnetic targeting of brain tumors. *Biomaterials* 2008;**29**:487-96.
9. Xie J, Liu G, Eden HS, Ai H, Chen X. Surface-engineered magnetic nanoparticle platforms for cancer imaging and therapy. *Acc Chem Res* 2011;**44**:883-92.
10. Bergemann C, Müller-Schulte D, Oster J, Brassard L à, Lübbe A. Magnetic ion-exchange nano- and microparticles for medical, biochemical and molecular biological applications. *J Magn Magn Mater* 1999;**194**:45-52.
11. Hadjipanayis CG, Bonder MJ, Balakrishnan S, Wang X, Mao H. Metallic Iron Nanoparticles for MRI Contrast Enhancement and Local Hyperthermia. *Small* 2008;**4**:1925-9.
12. Popescu RC, Andronescu E, Grumezescu AM. In vivo evaluation of Fe3O4 nanoparticles. *Rom J Morphol Embryol* 2014;**55**:1013-8.
13. Alexis F, Pridgen EM, Langer R, Farokhzad OC. *Handb Exp Pharmacol* 2010;**197**:55-86.
14. Branquinho LC, Carrião MS, Costa AS, Zufelato N, Sousa MH, Miotto R, et al. Effect of magnetic dipolar interactions on nanoparticle heating efficiency: implications for cancer hyperthermia. *Sci Rep* 2013;**3**:2887.
15. Lee J-H, Jang J-T, Choi J-S, Moon SH, Noh S-H, Kim J-W, et al. Exchange-coupled magnetic nanoparticles for efficient heat induction. *Nat Nanotechnol* 2011;**6**:418-22.
16. Huang HS, Hainfeld JF. Intravenous magnetic nanoparticle cancer hyperthermia. *Int J Nanomedicine* 2013;**8**:2521-32.
17. Lukianova-Hleb EY, Ren X, Sawant RR, Wu X, Torchilin VP, Lapotko DO. Ondemand intracellular amplification of chemoradiation with cancer-specific plasmonic nanobubbles. *Nat Med* 2014;**20**:778-84.
18. Sanhai WR, Sakamoto JH, Canady R, Ferrari M. Seven challenges for nanomedicine. *Nat Nanotechnol* 2008;**3**:242-4.
19. Gamarra LF, Pontuschka WM, Amaro Jr E, Costa-Filho AJ, Brito GES, Vieira ED, et al. Kinetics of elimination and distribution in blood and liver of biocompatible ferrofluids based on Fe3O4 nanoparticles: An EPR and XRF study. *Mater Sci Eng C* 2008;**28**:519-25.
20. Gobbo OL, Wetterling F, Vaes P, Teughels S, Markos F, Edge D, et al. Biodistribution and pharmacokinetic studies of SPION using particle electron paramagnetic resonance, MRI and ICP-MS. *Nanomedicine* 2015;**10**:1751-60.
21. Nie S. Understanding and overcoming major barriers in cancer nanomedicine. *Nanomedicine (Lond)* 2010;**5**:523-8.
22. Estevanato LLC, Lacava LM, Carvalho LCF, Azevedo RB, Silva O, Pelegrini F, et al. Long-term biodistribution and biocompatibility investigation of dextran-coated magnetite nanoparticle using mice as the animal model. *J Biomed Nanotechnol* 2012;**8**:301-8.
23. Jain TK, Reddy MK, Morales MA, Leslie-Pelecky DL, Labhasetwar V. Biodistribution, clearance, and biocompatibility of iron oxide magnetic nanoparticles in rats. *Mol Pharm* 2008;**5**:316-27.
24. Yu M, Zheng J. *Clearance Pathways and Tumor Targeting of Imaging Nanoparticles*; 20156655-74.
25. Ma HL, Xu YF, Qi XR, Maitani Y, Nagai T. Superparamagnetic iron oxide nanoparticles stabilized by alginate: Pharmacokinetics, tissue distribution, and applications in detecting liver cancers. *Int J Pharm* 2008;**354**:217-26.
26. Weissleder R, Nahrendorf M, Pittet MJ. Imaging macrophages with nanoparticles. *Nat Mater* 2014;**13**:125-38.
27. Shah NeB, Vercellotti GM, White JG, Fegan A, Wagner CR, Bischof JC. Bloodnanoparticle interactions and in Vivo biodistribution: Impact of surface peg and ligand properties. *Mol Pharm* 2012;**9**:2146-55.
28. Chatterjee DK, Wolfe T, Lee J, Brown AP, Singh PK, Bhattarai SR, et al. Convergence of nanotechnology with radiation therapy — insights and implications for clinical translation. *Transl Cancer Res* 2013;**2**:256-68.
29. Blanco E, Shen H, Ferrari M. Principles of nanoparticle design for overcoming biological barriers to drug delivery. *Nat Biotechnol* 2015;**33**:941-51.
30. Lee J-H, Huh Y-M, Jun Y-W, Seo J-W, Jang J-T, Song H-T, et al. Artificially engineered magnetic nanoparticles for ultra-sensitive molecular imaging. *Nat Med* 2007;**13**:95-9.
31. Gleich B, Weizenecker J. Tomographic imaging using the nonlinear response of magnetic particles. *Nature* 2005;**435**:1214-7.
32. Ferguson RM, Minard KR, Khandhar AP, Krishnan KM. Optimizing magnetite nanoparticles for mass sensitivity in magnetic particle imaging. *Med Phys* 2011;**38**:1619-26.
33. Liu Y, Welch MJ. Nanoparticles labeled with positron emitting nuclides: Advantages, methods, and applications. *Bioconjug Chem* 2012;**23**:671-82.
34. Marciani L. Assessment of gastrointestinal motor functions by MRI: A comprehensive review. *Neurogastroenterol Motil* 2011;**23**:399-407.
35. Miranda JR, Baffa O, de Oliveira RB, Matsuda NM. An AC biosusceptometer to study gastric emptying. *Med Phys* 1992;**19**:445-8.
36. Miranda JR, Oliveira RB, Sousa PL, Braga FJ, Baffa O. A novel biomagnetic method to study gastric antral contractions. *Phys Med Biol* 1997;**42**:1791-9.
37. Américo MF, Marques RG, Zandoná EA, Andreis U, Stelzer M, Corá LA, et al. Validation of ACB in vitro and in vivo as a biomagnetic method for measuring stomach contraction. *Neurogastroenterol Motil* 2010;**22**:1340-5.
38. Quini CC, Américo MF, Corá LA, Calabresi MF, Alvarez M, Oliveira RB, et al. Employment of a noninvasive magnetic method for evaluation of gastrointestinal transit in rats. *J Biol Eng* 2012;**6**:6.
39. Calabresi MFF, Quini CC, Matos JF, Moretto GM, Americo MF, Graça JRV, et al. Alternate current biosusceptometry for the assessment of gastric motility after proximal gastrectomy in rats: a feasibility study. *Neurogastroenterol Motil* 2015;**27**:1613-20.

40. Quini CC, Matos JF, Prósperoa AG, Calabresi MFF, Zufelato N, Bakuzis AF, et al. Renal perfusion evaluation by alternating current biosusceptometry of magnetic nanoparticles. *J Magn Magn Mater* 2015;**380**:2-6.
41. Baffa O, Oliveira RB, Miranda JRA, Troncon LEA. Analysis and development of AC biosusceptometer for orocaecal transit time measurements. *Med Biol Eng Comput* 1995;**33**:353-7.
42. Bastuscheck CM, Williamson SJ. Technique for measuring the ac susceptibility of portions of the human body or other large objects. *J Appl Phys* 1985;**58**:3896-906.
43. Bulte JWM. Hot spot MRI emerges from the background. *Nat Biotechnol* 2005;**23**:945-6.
44. Wunderbaldinger P, Josephson L, Weissleder R. Tat peptide directs enhanced clearance and hepatic permeability of magnetic nanoparticles. *Bioconjug Chem* 2002;**13**:264-8.
45. Gordon AC, Lewandowski RJ, Salem R, Day DE, Omary RA, Larson AC. Localized hyperthermia with iron oxide-doped yttrium microparticles: Steps toward imageguided thermoradiotherapy in liver cancer. *J Vasc Interv Radiol* 2014;**25**:397-404.
46. Kim HM, Lee H, Hong KS, Cho MY, Sung M-H, Poo H, et al. Synthesis and High Performance of Magnetofluorescent Polyelectrolyte Nanocomposites as MR / Near-Infrared Multimodal Cellular Imaging. *ACS Nano* 2011:8230-40.
47. Huang H, Delikanli S, Zeng H, Ferkey DM, Pralle A. Remote control of ion channels and neurons through magnetic-field heating of nanoparticles. *Nat Nanotechnol* 2010;**5**:602-6.
48. Rodrigues HF, Mello FM, Branquinho LC, Zufelato N, Silveira-Lacerda EP, Bakuzis AF. Real-time infrared thermography detection of magnetic nanoparticle hyperthermia in a murine model under a non-uniform field configuration. *Int J Hyperthermia* 2013;**29**:752-67.
49. Atkinson WJ, Brezovich I, Chakraborty DP. Usable frequencies in hyperthermia with thermal seeds. *IEEE Trans Biomed Eng* 1984;**31**:70-5.
50. Lacava LM, Lacava ZGM, Da Silva MF, Silva O, Chaves SB, Azevedo RB, et al. Magnetic resonance of a dextran-coated magnetic fluid intravenously administered in mice. *Biophys J* 2001;**80**:2483-6.
51. Gamarra LF, da Costa-Filho AJ, Mamani JB, Ruiz RC, Pavon LF, Sibov TT, et al. Ferromagnetic resonance for the quantification of superparamagnetic iron oxide nanoparticles in biological materials. *Int J Nanomedicine* 2010;**5**:203-11.
52. Chertok B, Cole AJ, David AE, Yang VC. Comparison of Electron Spin Resonance Spectroscopy and Inductively-Coupled Plasma Optical Emission Spectroscopy for Biodistribution Analysis of Iron-Oxide Nanoparticles. *Mol Pharm* 2010;**7**:375-85.
53. Koksharov YA, Gubin SP, Kosobudsky ID, Yurkov GY, Pankratov DA, Ponomarenko LA, et al. Electron paramagnetic resonance spectra near the spin-glass transition in iron oxide nanoparticles. 2000;**63**:1-4.
54. Silva AC, Bock NA. Manganese-enhanced MRI: An exceptional tool in translational neuroimaging. *Schizophr Bull* 2008;**34**:595-604.
55. O'Neal SL, Zheng W. Manganese Toxicity Upon Overexposure: a Decade in Review. *Curr Environ Health Rep* 2015;**2**:315-28.
56. Wilhelm S, Tavares AJ, Dai Q, Ohta S, Audet J, Dvorak HF, et al. Analysis of nanoparticle delivery to tumours. *Nat Rev Mater* 2016;**1**:1-12.
57. Bakuzis AF, Branquinho LC, Castro L Luiz E, de Amaral e Eloi MT, Miotto R. Chain formation and aging process in biocompatible polydisperse ferrofluids: Experimental investigation and Monte Carlo simulations. *Adv Colloid Interface Sci* 2013;**191–192**:1-21.
58. Salvador MA, Costa AS, Gaeti M, Mendes LP, Lima EM, Bakuzis AF, et al. Characterization, nanoparticle self-organization, and Monte Carlo simulation of magnetoliposomes. *Phys Rev E* 2016;**93**:22609.